

SCIENTIFIC REPORTS

OPEN

Change of the relative line strengths due to the resonance induced population transfer between Fe XVII and FeXVI ions

Chensheng Wu^{1,2} & Xiang Gao^{1,3}

We present a detailed study to resolve the discrepancy between the existing theoretically estimated oscillator strengths and the recently observed result from the X-ray free electron laser (XFEL) experiment performed at the Linac Coherent Light Source (LCLS) for the intensity ratio between two of the strongest emission lines from Ne-like Fe XVII (Fe¹⁶⁺) ion. By including the dynamic resonance induced population transfer due to autoionization between the coexisting Fe XVII and Fe XVI (Fe¹⁵⁺) ions in the XFEL experiment, we are able to successfully resolve this difference in theory and experiment. Further experimental works are suggested for a more detailed understanding of the dynamic resonance processes for ions.

The x-ray emission lines of the Ne-like Fe¹⁶⁺ ion have been observed in a variety of astrophysical objects, including the Sun, stellar coronae, elliptical galaxies, and supernova remnants^{1–4}. Two of the most intense lines of the Ne-like Fe¹⁶⁺ ion are the $2p^5 3d^1 P_1 \rightarrow 2p^6 S_0$ dipole emission line at 15.01 Å (3C) and the $2p^5 3d^1 D_1 \rightarrow 2p^6 S_0$ inter-combination line at 15.26 Å (3D). The wavelength separation of these two lines is large enough to be resolved by spectrometers with moderate resolving power, but, is small enough so that errors in spectrometer response are relatively small^{1–4}. However, the diagnostic utility of these two lines has been limited by the fact that although extensive studies have been carried out, discrepancies between the theoretical estimates and the measurements from astrophysical and laboratory sources persist^{5–7}.

In a recent benchmark experiment performed at the Linac Coherent Light Source (LCLS)⁵, the highly charged Fe ions were first generated in an electron beam ion trap (EBIT) and then photo-excited by the X-ray free electron laser (XFEL). This experiment was designed to allow a direct comparison of experimental and theoretical results, excluding the effects of electron collisions. The measured weighted 3C/3D ratio was 2.61 ± 0.23 , which is significantly lower than the most elaborated theoretical values at 3.4 or higher^{5–10}. It was concluded that the discrepancies are due to the inaccurate atomic wave functions^{5,11}. This conclusion appears to be supported by a recent configuration interaction calculation with some fine-tuning parameters¹². However, it was argued later that the calculated ratio in ref.¹² is unreliable due to a limited and unbalanced treatment of electron correlations¹³. Alternatively, it was proposed that other physical processes beyond those included in the atomic structure calculation of an isolated atomic system, such as the one due to the ultra-high intensities of XFEL with ultra-short pulse period, may be responsible for this discrepancy^{10,14,15}. By scrutinizing the experimental conditions at the LCLS^{5,11,16–18}, the intensities of the XFEL pulses are not sufficiently high to support this proposed interpretation^{10,14,15} and it is not likely that the discrepancy between theory and experiment could be attributed to the high order nonlinear effect. Thus, it is worth exploring further other possibilities to explain the experiment⁵.

Our investigation starts with a critical assessment of the theoretical intensity ratio based on an atomic structure calculation of isolated ion with a revised multi-configuration Dirac-Fock (MCDF) approach, where the quasi-complete basis scheme is adopted to optimize the atomic orbitals (AOs) using the GRASP-JT version^{19,20} based on the earlier GRASP2K codes^{21,22}. In this way, the convergence of the atomic structures can be examined step by step with limited computational efforts. This approach was developed recently to study the forbidden transitions in O⁺ ion with its result within the overlap range of two available astrophysical observations and with a

¹Beijing Computational Science Research Center, Beijing, 100193, China. ²Department of Engineering Physics, Tsinghua University, Beijing, 100084, China. ³Center for Computational Sciences, University of Tsukuba, 1-1-1 Tennodai, Tsukuba, Ibaraki, 305-8577, Japan. Correspondence and requests for materials should be addressed to X.G. (email: xgao@csrc.ac.cn)

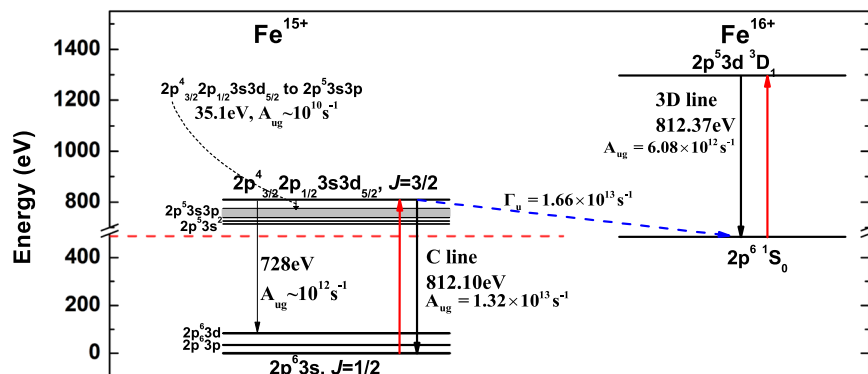


Figure 1. The energy levels and transitions of Fe XVI (Fe^{15+}) and Fe XVII (Fe^{16+}). The bold red arrows represent the excitation process of the XFEL. The bold black arrows represent the C and 3D emission lines. The thin black arrows represent some minor decay channels of the $2p^4_{3/2}2p_{1/2}3s3d_{5/2}$ $J = 3/2$ resonant state. The blue dash arrow represents the autoionization from the Fe XVI. The red horizontal dash line represents the first ionization threshold at 489.31 eV of Fe XVI.

very small theoretical uncertainty¹⁹. With a converged 3C/3D ratio of 3.567 ± 0.003 from our detailed calculation, there is definitely the need to explore other possible physical effects which might bring the theoretical ratio close to the one observed recently by the XFEL experiment.

There are three known emission lines from the upper states of Fe XVI ions (Fe^{15+}) to its ground state $2p^6 3s_{1/2}$ $J = 1/2$, i.e., line A from $2p^4_{3/2}2p_{1/2}3s3d_{3/2}$ $J = 3/2$ state, line B from $2p^4_{3/2}2p_{1/2}3s3d_{5/2}$ $J = 1/2$ state and line C from $2p^4_{3/2}2p_{1/2}3s3d_{5/2}$ $J = 3/2$ state^{23,24}. It is also known from the previous EBIT experiment that the C line blends with the 3D line of Fe XVII (Fe^{16+}) since both have an energy close to 812 eV (indicated by the bold black arrows shown in Fig. 1)^{23,24}. In the LCLS experiment, the contribution of the Fe XVI C line was subtracted from the Fe XVII spectra for the 3D line with the assumption that the emissions from Fe XVII and Fe XVI are independent⁵. It turns out that in addition to the radiative decays, this upper state of the C line from Fe XVI could also autoionize into the ground state of Fe XVII shown by the blue dash arrow in Fig. 1. Since there was a finite pulse duration of the LCLS experiment, the resulting Fe XVII in its ground state could then be excited to increase the population of the upper level of the Fe XVII 3D line and thus increases the intensity of the 3D line. On the other hand, with the XFEL photon energy at the position of the Fe XVII 3C line, there is no resonant autoionization states of the Fe XVI ion. Considering the direct photon ionization probability is several orders of magnitude lower than the resonant autoionization process, the population of the upper level of the Fe XVII 3C line will not be influenced by the Fe XVI ion and thus the intensity of 3C line will not be changed. Then a decrease of the measured 3C/3D line ratio could be expected.

In this paper, we study such resonance induced population transfer process between Fe XVI and Fe XVII ions in detail, which may offer a reasonable explanation for the discrepancy between theory and experiment. We will first discuss the assessment of the theoretical 3C and 3D oscillator strengths of Fe XVII ion, and then presents the results of our study of the resonance induced population transfer process. Finally, the implications of the present work are summarized.

Results and Discussions

The assessment of the theoretical 3C and 3D oscillator strengths of Fe XVII ion. The calculation of the atomic structure of the Fe XVII (Fe^{16+}) ion is based on the well-established full relativistic multi-configuration Dirac-Fock (MCDF) approach^{21,22}. In the present study, the oscillator strengths of the transitions between the ground state and the first five $J^\pi = 1^-$ excited levels of the Fe XVII are calculated together to guarantee the final convergence of the 3C and 3D lines. The quasi-complete basis scheme is adopted to optimize the atomic orbitals (AOs) using the GRASP-JT version^{19,20} based on the earlier GRASP2K codes^{21,22}. In this way, the convergence of the atomic structures can be examined step by step with limited computational efforts.

We started with the atomic orbitals (AOs) with principal quantum number $n = 1, 2, 3$ and $(n-l-1)$ nodes that are optimized by multi-configuration self-consistent-field (MCSCF) iterations to minimize the lowest 37 energy levels of $2p^6$, $2p^5 3s$, $2p^5 3p$, and $2p^5 3d$ states to form the *zeroth* level basis. With the AOs fixed up to $n = 3$, the pseudo AOs with $n = 4$ are obtained by further MCSCF iterations to optimize the statistic weights of the ground state and the first five $J^\pi = 1^-$ excited levels of the Fe XVII to generate the *first* level basis. The additional electronic configurations from the $2p^6$, $2p^5 3s$, $2p^5 3p$, and $2p^5 3d$ reference configurations with $n = 3$ and 4 AOs (i.e., two electrons excited from the core shell and one electron excited from the valence shell) are added in our calculation to include single, double, and some important triple excitations, even those from the 2s inner shells. In succession, by adding more and more AOs in what we termed as the quasi-complete basis, we have included in the present calculation to *sixth* level basis with $n_{\max} = 9$.

Based on these AO basis, the energy levels and corresponding transition rates are calculated by the configuration interaction (CI) method with more configurations than previous MCSCF calculations where the double excitations of the 2s inner shell are allowed. So the CI calculations take account of all the valence- and prominent core excitation correlations, which are important for convergence. In fact, with $n = 9$, there are a total of over 3.7

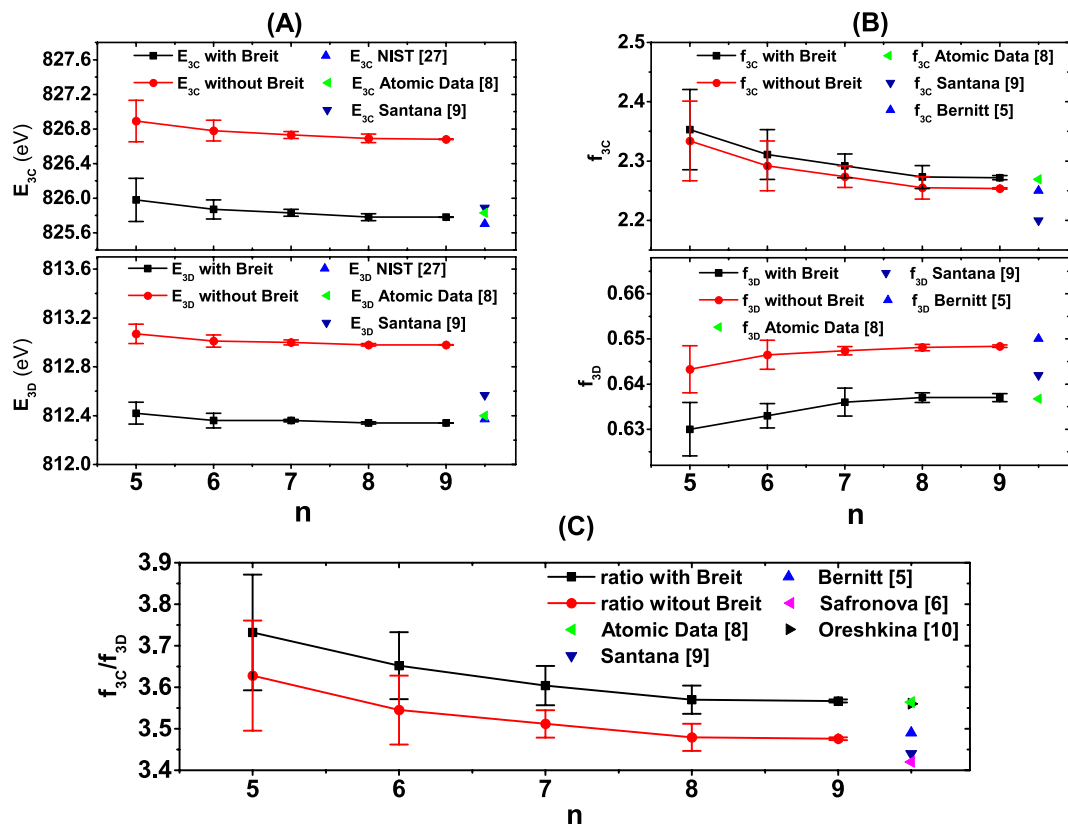


Figure 2. The variation of the excitation energies E_{3C} , E_{3D} , the oscillator strengths f_{3C} , f_{3D} , and the intensity ratio f_{3C}/f_{3D} , with and without the Breit interaction, as the size of the quasi-complete basis increases with n in our MCDF calculation. Comparisons with other available atomic structure calculations are also presented.

Configuration	E^{DCa}	$E^{DC+Breit b}$	$E^{NIST c}$	f^{DCa}	$f^{DC+Breit b}$	$f^{Ref d}$
$(2p^5)_{3/2}3s_{1/2}$	727.444(5)	727.018(5)	727.139	0.123(1)	0.123(1)	0.122
$(2p^5)_{1/2}3s_{1/2}$	739.681(5)	738.941(6)	739.054	0.101(1)	0.103(1)	0.101
$(2p^5)_{3/2}3d_{3/2}$	802.835(3)	802.271(3)	802.401	0.010(1)	0.010(1)	0.010
$(2p^5)_{3/2}3d_{5/2}$ (3D)	812.982(1)	812.343(1)	812.369	0.648(1)	0.637(1)	0.637
$(2p^5)_{1/2}3d_{3/2}$ (3C)	826.685(2)	825.782(2)	825.700	2.254(1)	2.272(4)	2.269

Table 1. The calculated excitation energies (in eV) of the first five $J^P = 1^-$ levels from the ground state of Fe XVII and their oscillator strength. ^aThe calculations with Dirac-Coulomb Hamiltonian. ^bThe calculations with Dirac-Coulomb Hamiltonian, Breit interactions and other high order QED corrections. ^cThe experimental values from NIST database²⁷. ^dThe MCDF calculation results from ref.⁸.

million electronic configurations in our CI calculations. The QED corrections, especially the Breit interaction^{25,26}, are added to the atomic Hamiltonian as a perturbation in the CI calculations. The Breit interaction is the most important high-order correction not only for the energy levels but also for the transition rates. The uncertainties of our calculated transition energies are estimated from the difference between CI calculations with AOs of adjacent n . The uncertainties of our calculated oscillator strengths are estimated by combining both the difference between CI calculations with AOs of adjacent n , as well as the difference between length and velocity gauge. Figure 2 shows the convergent behaviors of excitation energies E , oscillator strengths f and the oscillator strengths ratio of 3C and 3D with estimated uncertainties of various AO bases, compared with some reference data^{5,6,8-10,27}. Table 1 presents the final calculation values using the quasi-complete basis (i.e., AOs with $n=9$), compared with some reference data^{8,27}.

In addition to the excellent agreement between the length and velocity results of our theoretical oscillator strength f_{3C} and f_{3D} , our calculated excitation energy E , f_{3C} , f_{3D} , and the ratio f_{3C}/f_{3D} are indeed influenced by one of the most important QED corrections, the Breit interaction^{25,26}. By including the Breit correction, the excitation energies from the current calculation are less than 0.02% from the NIST data²⁷. The f_{3C}/f_{3D} ratio changes from a value of 3.476 ± 0.003 to 3.567 ± 0.003 since the value of f_{3C} increases while the value of f_{3D} decreases after the Breit interaction was taken into account. With a converged ratio from our detailed calculation in close agreement with other existing atomic structure calculations⁵⁻¹⁰, we then conclude that other physics must be responsible for the discrepancy between previous theory and experiment.

Theoretical model for resonance induced population transfer process. To study the resonance induced population transfer process between the Fe XVI and Fe XVII ions, we note first that, quantitatively, the time scale of the emission process of photon is usually of the order of 100–1000 fs, whereas the electron processes, such as the collision ionization (CI), the radiative recombination (RR), the dielectronic recombination (DR), and the excitation autoionization (EA) in the EBIT are typically of the order of 10^{-3} s^{28–30}. Second, the XFEL photon energy was continuously scanned with a repetition rate of 120 Hz (Supplementary of ref.⁵), which means after the interaction with the XFEL, the ions in the EBIT have adequate time to return to their equilibrium stable state. Therefore, we could decouple those electron processes from the photon process when we discuss this XFEL photon related resonance induced population transfer process. By including the dominant decay channel (i.e., to the ground state of Fe XVI, which will be discussed later) and the autoionization of Fe XVI into the ground state of Fe XVII, the rate equations for the population densities for the ground and excited states of Fe XVI and Fe XVII ions with incident XFEL photon energies $\hbar\omega$ around 812 eV (the C and 3D lines) could then be expressed as:

$$\begin{aligned} \frac{d}{dt}N_g^{Fe^{15+}}(t) &= N_u^{Fe^{15+}}(t)B_{ug}^{Fe^{15+}}(\omega_C)\rho(\omega) + N_u^{Fe^{15+}}(t)A_{ug}^{Fe^{15+}}(\omega_C) \\ &\quad - N_g^{Fe^{15+}}(t)B_{gu}^{Fe^{15+}}(\omega_C)\rho(\omega), \end{aligned} \quad (1A)$$

$$\begin{aligned} \frac{d}{dt}N_u^{Fe^{15+}}(t) &= -N_u^{Fe^{15+}}(t)B_{ug}^{Fe^{15+}}(\omega_C)\rho(\omega) - N_u^{Fe^{15+}}(t)A_{ug}^{Fe^{15+}}(\omega_C) \\ &\quad + N_g^{Fe^{15+}}(t)B_{gu}^{Fe^{15+}}(\omega_C)\rho(\omega) - N_u^{Fe^{15+}}(t)\Gamma_u^A, \end{aligned} \quad (1B)$$

$$\begin{aligned} \frac{d}{dt}N_g^{Fe^{16+}}(t) &= N_u^{Fe^{16+}}(t)B_{ug}^{Fe^{16+}}(\omega_{3D})\rho(\omega) + N_u^{Fe^{16+}}(t)A_{ug}^{Fe^{16+}}(\omega_{3D}) \\ &\quad - N_g^{Fe^{16+}}(t)B_{gu}^{Fe^{16+}}(\omega_{3D})\rho(\omega) + N_u^{Fe^{15+}}(t)\Gamma_u^A, \end{aligned} \quad (1C)$$

$$\begin{aligned} \frac{d}{dt}N_u^{Fe^{16+}}(t) &= -N_u^{Fe^{16+}}(t)B_{ug}^{Fe^{16+}}(\omega_{3D})\rho(\omega) - N_u^{Fe^{16+}}(t)A_{ug}^{Fe^{16+}}(\omega_{3D}) \\ &\quad + N_g^{Fe^{16+}}(t)B_{gu}^{Fe^{16+}}(\omega_{3D})\rho(\omega), \end{aligned} \quad (1D)$$

where the transition rate A_{ug} is the Einstein A coefficients from the upper level to the lower level, B_{ug} and B_{gu} are the Einstein B coefficients with $B_{ug} = (\pi^2 c^3 / \hbar \omega^3) A_{ug}$, and Γ_u^A is the autoionization rate of Fe XVI ion. $\rho(\omega) = I_p / (c \Delta \omega \sqrt{2\pi}) \exp[-(\omega - \omega_k)^2 / 2 \Delta \omega^2]$, where I_p is the peak intensities of XFEL around energy ω_k , $\Delta \omega$ is the line width of the XFEL with the assumption of Gaussian profile, ω_k is the resonant energy of the respective transition, and c is the speed of light³¹. The initial conditions of the equations are $N_u^{Fe^{16+}}(t=0) = 0$, $N_u^{Fe^{15+}}(t=0) = 0$ with $N_g^{Fe^{15+}}(t=0) / N_g^{Fe^{16+}}(t=0)$ as the concentration ratio between Fe XVI and Fe XVII ions in the EBIT. For other XFEL photon energies between 810 eV and 830 eV where the Fe XVII and Fe XVI lines are well separated, the rate equations are simpler. More specifically, around the resonant energies of the Fe XVI A and B lines, only Eqs (1A) and (1B) are needed (with ω_c replaced by ω_A and ω_B , respectively), whereas for the Fe XVII 3C line, only Eqs (1C) and (1D) are needed (without the last autoionization term and with ω_{3D} replaced by ω_{3C}).

After solving Eq. (1) at a specific XFEL photon energy ω_0 with peak intensity I_p for time-dependent population of the upper level of Fe XVII $N_u^{Fe^{16+}}(t)$ and Fe XVI $N_u^{Fe^{15+}}(t)$, the total fluorescence photon number $N_{ph}^i(I_p, \omega_0)$ is given by,

$$N_{ph}^i(I_p, \omega_0) = \int_0^\tau N_u^i(t) A_{ug}^i(\omega_0) dt + N_u^i(\tau) \beta^i, \quad (2)$$

where τ is the incident XFEL pulse duration, i represents the Fe XVI or Fe XVII ion respectively and β^i is the transition branching ratio, which equals 1 for Fe XVII and $A_{ug}^{Fe^{15+}} / (A_{ug}^{Fe^{15+}} + \Gamma_u^A)$ for Fe XVI. The first term represents the emitted photons during the pulse period, the second is the remaining emitted photons at the end of the pulse. Note that only the spontaneous emission is relevant for the fluorescence because the photons emitted from stimulated radiation have the same direction as incident laser, which are not detected by the detectors perpendicular to the incident laser⁵. The anisotropic angular distributions are also taken into account in present simulations.

The parameters used in the simulation. All required transition rates between 810 eV and 830 eV for the Fe XVII ions have already been obtained from the extended MCDF calculation discussed earlier. For the Fe XVI ion, the transition rates are calculated with the well-established atomic structure theories such as the relativistic eigenchannel R-matrix method detailed elsewhere^{20,32}. In particular, for the autoionization rate, our calculation has taken into account fully the interaction between various resonant states and the continua. The relevant transition and autoionization rates are, respectively, $0.87 \times 10^{13} \text{ s}^{-1}$ and $3.92 \times 10^{13} \text{ s}^{-1}$ for the A line, $2.45 \times 10^{13} \text{ s}^{-1}$ and $2.13 \times 10^{12} \text{ s}^{-1}$ for the B line, and $1.32 \times 10^{13} \text{ s}^{-1}$ and $1.662 \times 10^{13} \text{ s}^{-1}$ for the C line. In addition, the radiative decay from the upper $2p_{3/2}^4 3d_{5/2} 3s_{3/2} 3d_{5/2} J = 3/2$ state is dominated by C line with its decay rate at least one order of magnitude greater than the other decays channels (including various cascade decay processes) as shown in

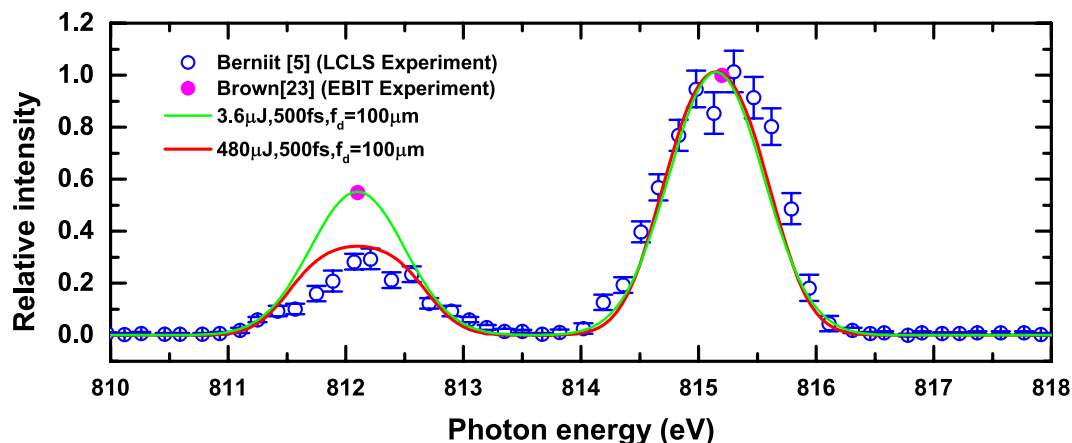


Figure 3. Comparison of the experimentally observed spectra of Fe XVI ions to our simulated spectra with (1) $P_E = 3.6 \mu\text{J}$, $\tau = 500 \text{ fs}$, and $f_d = 100 \mu\text{m}$ and (2) $P_E = 0.48 \text{ mJ}$, $\tau = 500 \text{ fs}$, and $f_d = 100 \mu\text{m}$.

Fig. 1. At specific photon energy, only the dominant decay channel and the autoionization of Fe XVI into the ground state of Fe XVII (if it contributes to the change in the Fe XVII population) are included when solving the rate equations.

We then examine briefly the relevant XFEL parameters in the LCLS experiment⁵ which we will apply in the numerical simulation presented later. For the line width parameter $\Delta\omega$ of the XFEL photons, we use the value of 0.4 eV in all our simulations, which will result in a good match with the experimental spectra resolution⁵. The photon intensity I_p used in the simulations can be obtained from pulse energy P_E , pulse duration τ and the effective focal area $\sigma_d = f_d^2$ with f_d the focal diameter of the photon beam by $I_p = P_E / (\tau \sigma_d)$. Unfortunately, these three parameters were not well defined in the experiment⁵, we can only infer the ranges of them from the LCLS specifications^{11,16–18,33,34}. The raw X-ray pulse energy before the monochromator is about 1–4 mJ^{11,16}. The final pulse energies reaching the experimental end stations after the monochromator range from 0.8 μJ for 500 eV photons to 0.48 mJ for 1000 eV photons^{33,34}. According to ref.¹¹, the pulse duration τ for the XFEL ranges from 50 to 500 fs. For the focal diameter f_d of the photon beam, the unfocused beam size is in the range 1–3 mm^{17,33,34} with the focusing capability to about 2 μm ^{17,33}. Since it was stated in the Supplementary of ref.⁵ that “a very weakly focused photon beam” was used in the LCLS experiment and it is also reasonable to expect an adequate overlap between the XFEL photons with the EBIT ions in the diameter 0.5 mm (Supplementary of ref.⁵), we assume a larger f_d (e.g., from 25 μm to 250 μm) in our numerical simulations, which may be closer to the actual experiment conditions.

The results of pure Fe XVI ion. To examine the effect of the autoionization to the upper state population of the Fe XVI C line, we first focus our study on the simulation of the Fe XVI only spectrum shown in Fig. (3B) of ref.⁵ by solving Eqs (1A) and (1B). Figure 3 compares the experimentally observed spectra to our simulated spectra at two sets of XFEL pulse parameters. At lower pulse energy, our simulated spectrum is in good agreement with the previous EBIT experiment using electron excitation by Brown *et al.*²³. Its higher intensity ratio of over 0.5 between the C and B lines mainly reflects the branching ratio between the C and B lines that is determined by the atomic transition rates, with little population loss of the C line. On the other hand, as expected, the intensity ratio of the C and B lines decreases from over 0.5 at lower XFEL power to 0.3 at higher XFEL power with a substantial population loss of the upper state of C line due to the autoionization and thus a much closer agreement with the observed spectrum from Fig. (3B) of ref.⁵. Accordingly, what is shown in Fig. 3 may offer the possibility of an experimental verification of the reliability of the theoretically estimated autoionization rate employed in our simulation should the values of pulse energy, duration and effective focal diameters are measured. The result in Fig. 3 also indicates that, in the XFEL pulse duration, the autoionized Fe XVII ion did not effectively survive in the EBIT under the condition to produce “pure” Fe XVI ion. On the other hand, under the EBIT condition where the Fe XVI and Fe XVII ions can co-exist, it is expected that the autoionized Fe XVII ion should survive in the EBIT during the XFEL pulse. This slight difference in the EBIT for the two measurement implies one should be careful about the subtraction of the C line contribution from the mixed spectra for the intensity of Fe XVII 3D line.

The results of the mixed Fe XVI and Fe XVII ions. We now turn our discussion to the combined Fe XVI and Fe XVII system. To simulate the experimental spectra of the mixture (Fig. (3A) of ref.⁵), the initial relative abundance between Fe XVII and Fe XVI ions in the EBIT is required. Since the autoionization of the Fe XVI B line is almost negligible, we can use the intensity ratio of Fe XVI B line and Fe XVII 3C line to determine this relative abundance, which is about 1.5 from ref.⁵. After considering the angular distribution differences²³ of these two lines, the ratio is corrected to 1.73. Then, by solving the related rate equations discussed above, the ion abundance of Fe XVI and Fe XVII is determined to be around 5:1. Figure 4(A) compares our simulated spectra with the experimentally observed spectrum. We start our discussion by first examining two

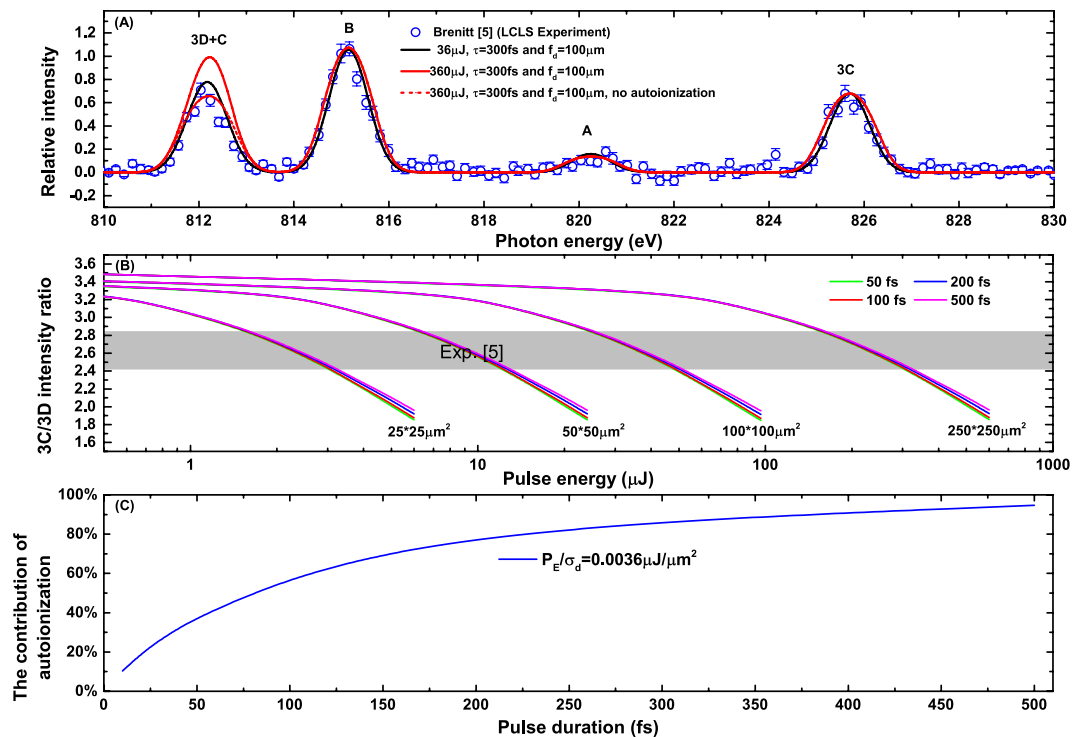


Figure 4. The resonance induced population transfer effects of the mixing Fe^{15+} and Fe^{16+} ions. (A) Comparison of the experimentally observed spectra of the mixing Fe^{15+} and Fe^{16+} ions to our simulated spectra. (B) The intensity ratios of 3C/3D by considering the autoionization of Fe^{15+} ions with various XFEL pulse parameters. (C) The contribution of autoionization for 3C/3D ratio of 2.6 with various pulse durations.

spectra simulated at pulse parameters of $P_E = 360 \mu\text{J}$, $\tau = 300 \text{ fs}$ and $f_d = 100 \mu\text{m}$ with and without autoionization shown by the red solid and red dash curves, respectively. As expected, these two simulated spectra are nearly identical for the B and A lines for the Fe XVI ion and the 3C line for the Fe XVII ion. In contrast, the substantial difference between these two curves for the combined 3D and C lines near 812 eV demonstrates clearly the effect of the population transfer from the upper state of the Fe XVI C line to the ground state of Fe XVII due to autoionization. Also shown in Fig. 4(A) by the dark solid curve is our simulated spectrum with two same pulse parameters $\tau = 300 \text{ fs}$ and $f_d = 100 \mu\text{m}$, but, at smaller energy $P_E = 36 \mu\text{J}$. The fact that this simulated spectrum is in very close agreement with the observed spectra supports strongly the reliability of the atomic data (such as the transition rates for Fe XVII and Fe XVI ions) and the simulation based on the rate equations employed in the present study. By taking into account the autoionization from the upper state of Fe XVI to the ground state of Fe XVII, as shown by the solid dark curve in Fig. 4(A), our simulated line ratio $R = N_{ph}^{Fe^{16+}}(I_p, \omega_{3C})/N_{ph}^{Fe^{16+}}(I_p, \omega_{3D})$, where $N_{ph}^{Fe^{16+}}(I_p, \omega_{3C})$ and $N_{ph}^{Fe^{16+}}(I_p, \omega_{3D})$ are calculated from Eq. (2) with the complete solution of Eq. (1), is expected to yield the intensity ratio of the 3C and 3D lines observed experimentally. Figure 4(B) presents the variation of the simulated 3C/3D intensity ratio with various possible XFEL parameter combinations. It is interesting to note that the 3C/3D ratio decreases as the pulse energy increases with the same focal diameter f_d due to the stronger autoionization effect. Similarly, the 3C/3D ratio decreases significantly, again i.e., with stronger autoionization effect, as photon intensity I_p increases at the same pulse energy P_E with smaller effective focal diameter f_d . On the other hand, with the same pulse energy and focal diameter, the 3C/3D ratio does not change significantly with pulse duration varying from 50 fs to 500 fs, which suggests that the ratio depends mostly on the P_E/σ_d .

For the sake of further analysis and considering the lifetime of the Fe XVI C line about 60 fs which is comparable with some XFEL pulse durations it is worth to separate the contribution of resonance induced population transfer effect from our simulations by, $P^{AI} = (R^{\text{no-AI}} - R^{AI})/(R^{\text{atomic}} - R^{AI})$, where $R^{\text{atomic}} = 3.567$ is the calculated 3C/3D ratio of the isolated Fe XVII ion; R^{AI} , $R^{\text{no-AI}}$ are the simulated line ratio, with and without the autoionization terms in Eq. (1), respectively. Figure 4(C) shows the P^{AI} of a fixed P_E/σ_d value that corresponds to the experimental measured ratio of 2.61 with various pulse durations. We can clearly see that with the pulse duration time less than 20 fs, or, substantially smaller than the lifetime of the Fe XVI C line, the contribution from the autoionization of the Fe XVI ion is small. For those XFEL parameters, the decrease of 3C/3D ratio should be attributed to the non-equilibrium effects discussed in refs^{14,15}. By contrast, with the pulse durations longer than 90 fs (in consistent with the typical LCLS X-ray pulse parameters^{11,16,17,33}), the resonance induced population transfer effect contributes more than a half. For example, for the pulse duration of 400 fs, where the high order nonlinear effects should be small, the contribution of the resonance induced population transfer effect is dominant, with P^{AI} over 90%.

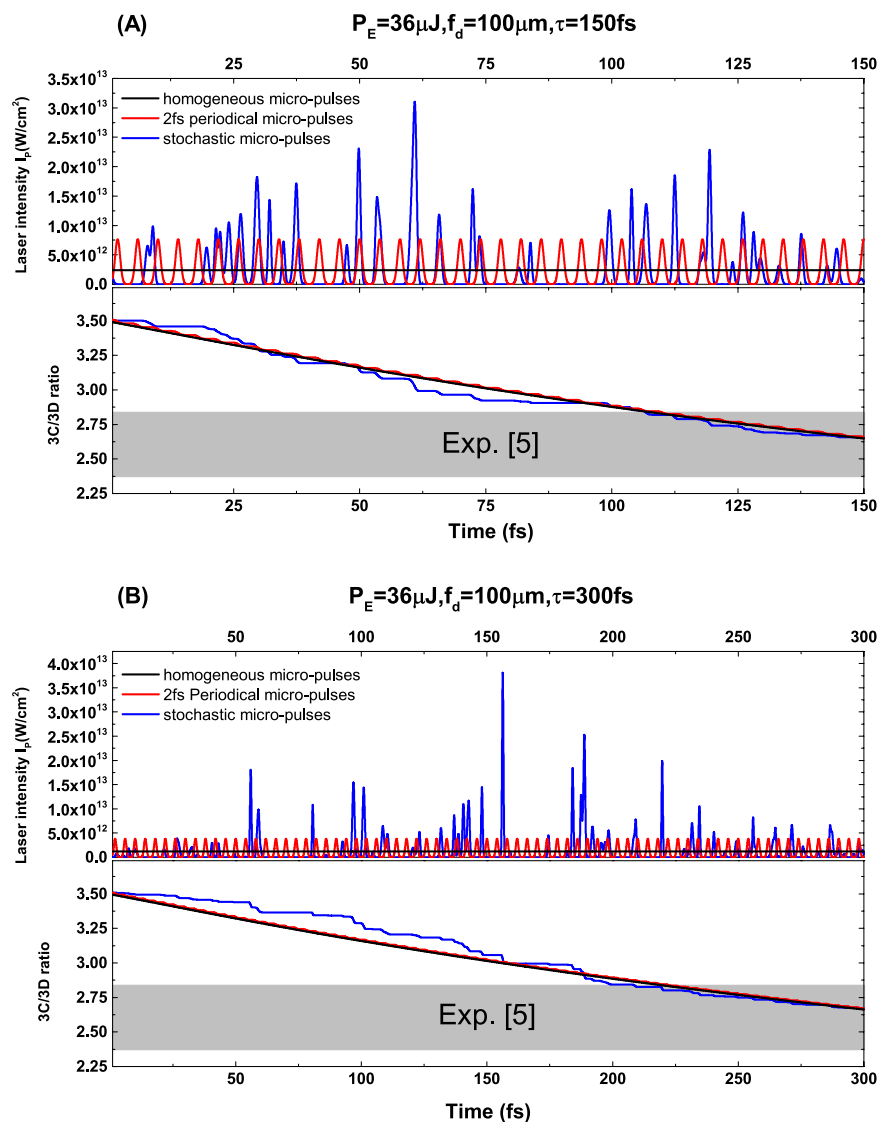


Figure 5. The variation of the 3C/3D ratio within the pulse duration. **(A)** The results for XFEL pulse parameter with pulse energy $P_E = 36 \mu\text{J}$, focal diameter $f_d = 100 \mu\text{m}$, and pulse duration $\tau = 150 \text{ fs}$. The upper panel exhibits the three different pulse substructures: homogeneous micro-pulses in black, the periodical micro-pulses with the period of 2 fs in red, and the stochastic micro-pulses in blue. The lower panel exhibits the simulated time dependent 3C/3D ratio with respect to these three pulse substructures. **(B)** The results for another XFEL pulse with the same P_E and f_d parameters as those in **(A)**, but with a different pulse duration $\tau = 300 \text{ fs}$.

The influence of the stochastic substructure of the XFEL pulses on theoretical simulations.

Due to the stochastic nature of the self-amplified stimulated emission (SASE) process, the pulse intensity of the XFEL is not homogeneous, which consists of sharp and stochastic individual pulses of 1–2 fs in duration with similar sized random gaps between the spikes^{35–37}. We now discuss the influence of these stochastic substructure of the XFEL pulses on our simulation results. As an illustration example, we choose $P_E/\sigma_d = 0.0036 \mu\text{J}/\mu\text{m}^2$ for the XFEL pulses [the same with the one in Fig. 4(C)]. With this pulse parameter, three typical substructures were considered in the simulations, i.e., (1) the homogeneous micro-pulses (constant photon intensity), (2) the periodical micro-pulses with the period of 2 fs, and (3) the stochastic micro-pulses. Figure 5(A) shows the corresponding results for the XFEL pulse with the duration $\tau = 150 \text{ fs}$. For these three different pulse substructures, the time variations of the simulated 3C/3D line ratio are almost identical, especially at the end of the pulse, which are all in good agreement with the experimental measurement⁵. Figure 5(B) shows the results for another different XFEL pulse with 300 fs duration. Similarly, the behavior of the 3C/3D ratio is also nearly independent with different pulse substructures. Therefore, we can make the conclusion that the final 3C/3D ratio mainly depends on the ratio of P_E/σ_d , the stochastic substructure of the XFEL pulses should have negligible effects on the 3C/3D ratio.

Conclusion

In summary, with an extended large scale full relativistic configuration interaction calculation including the quantum electrodynamics (QED) term such as the Breit interaction, we first came to the conclusion that the reliability of the theoretical results for isolated Fe XVII ions from the present calculation and other earlier atomic structure calculations may not be the cause for the discrepancy between the experimentally observed intensity ratio and the theoretical estimates. Since it is known that the energies of the Fe XVII 3D line and the Fe XVI C line are both close to 812 eV and the pulse length of the XFEL experiment is sufficiently longer than the time scale of the autoionization process transferring the upper state of the Fe XVI ion to the ground state of Fe XVII ion, we decided to focus our investigation on the dynamic resonance induced population transfer from Fe XVI to Fe XVII. By solving the relevant rate equations, we are able to generate theoretically simulated spectra as well as the intensity ratio in agreement with the experimental spectra from the LCLS experiment shown in Fig. 3 of ref.⁵. Note that we have also considered the influence of the plasma environment in the EBIT. Although the plasma screening will induce a substantial decrease in the ratio 3C/3D, it could not be the one responsible for the disagreement between theory and experiment due to the low electron densities^{38,39}.

In addition to resolving the discrepancy on intensity ratio discussed above, the conclusion from the present study may be examined by either performing the measurements of Fe XVI and Fe XVI/Fe XVII mixture under the well characterized XFEL intensity or with additional experiments for other Ne-like ions in the absence of the resonance induced population transfer. For example, based on our simulations, the measured ratio mainly depends on the ratio of the pulse energy and the effective focal area, i.e., P_E/σ_{db} for which some diagnostics are being developed at the LCLS^{40,41}. On the other hand, some attenuators¹⁸ may be used to reduce the XFEL intensity where the resonance induced population transfer effect is negligible, or alternatively, one can extract the pure Fe XVII ion from the EBIT known as the Electron Beam Ion Sources (EBIS)⁴² for the experiment.

Data Availability

The datasets generated during and/or analysed during the current study are available from the corresponding author on reasonable request.

References

1. Paerels, F. B. S. & Kahn, S. M. High-Resolution X-Ray Spectroscopy with Chandra and XMM-Newton. *Annu. Rev. Astron. Astrophys.* **41**, 291–342 (2003).
2. Behar, E., Cottam, J. & Kahn, S. M. The Chandra Iron-L X-Ray Line Spectrum of Capella. *Astrophys. J.* **548**, 966–975 (2001).
3. Xu, H. *et al.* High-Resolution Observations of the Elliptical Galaxy NGC 4636 with the Reflection Grating Spectrometer on Board XMM-Newton. *Astrophys. J.* **579**, 600–606 (2002).
4. Diaz Trigo, M. *et al.* Baryons in the relativistic jets of the stellar-mass black-hole candidate 4U 1630-47. *Nature* **504**, 260–262 (2013).
5. Bernitt, S. *et al.* An unexpectedly low oscillator strength as the origin of the Fe XVII emission problem. *Nature* **492**, 225–228 (2012).
6. Safronova, U. I., Namba, C., Murakami, I., Johnson, W. R. & Safronova, M. S. Electric-dipole, electric-quadrupole, magnetic-dipole, and magnetic-quadrupole transitions in the neon isoelectronic sequence. *Phys. Rev. A* **64**, 012507 (2001).
7. Chen, G. X. & Pradhan, A. K. Influence of Resonances on Spectral Formation of X-Ray Lines in Fe XVII. *Phys. Rev. Lett.* **89**, 013202 (2002).
8. Jönsson, P. *et al.* Relativistic CI calculations of spectroscopic data for the $2p^6$ and $2p^53l$ configurations in Ne-like ions between Mg III and Kr XXVII. *At. Data Nucl. Data Tables* **100**, 1–154 (2014).
9. Santana, J. A., Lepson, J. K., Träbert, E. & Beiersdorfer, P. Electron-correlation effects on the 3C to 3D line-intensity ratio in the Ne-like ions Ar^{8+} to Kr^{26+} . *Phys. Rev. A* **91**, 012502 (2015).
10. Oreshkina, N. S., Cavaletto, S. M., Keitel, C. H. & Harman, Z. Astrophysical line diagnosis requires nonlinear dynamical atomic modeling. *Phys. Rev. Lett.* **113**, 143001 (2014).
11. Bostedt, C. *et al.* Linac Coherent Light Source: The first five years. *Rev. Mod. Phys.* **88**, 015007 (2016).
12. Mendoza, C. & Bautista, M. A. Theoretical confirmation of the low Experimental 3C/3D f -value ratio in Fe XVII. *Phys. Rev. Lett.* **118**, 163002 (2017).
13. Wang, K. *et al.* Comment on “Theoretical Confirmation of the Low Experimental 3C/3D f -Value Ratio in Fe XVII”. *Phys. Rev. Lett.* **119**, 189301 (2017).
14. Loch, S. D., Balance, C. P., Li, Y., Fogle, M. & Fontes, C. J. Non-equilibrium Modeling of the Fe XVII 3C/3D Line Ratio in an Intense X-Ray Free-Electron Laser Excited Plasma. *Astrophys. J. Lett.* **801**, L13 (2015).
15. Li, Y., Fogle, M., Loch, S. D., Balance, C. P. & Fontes, C. J. Non-Equilibrium Modeling of the Fe XVII 3C/3D ratio for an Intense X-ray Free Electron Laser. *Can. J. Phys.* **95**, 869–877 (2017).
16. Emma, P. *et al.* First lasing and operation of an ångström-wavelength free-electron laser. *Nat. Photon.* **4**, 641–647 (2010).
17. Ferguson, K. R. *et al.* The Atomic, Molecular and Optical Science instrument at the Linac Coherent Light Source. *J. Synchrotron Rad.* **22**, 492–497 (2015).
18. Krzywinski, J. *et al.* Damage thresholds for blaze diffraction gratings and grazing incidence optics at an X-ray free-electron laser. *J. Synchrotron Rad.* **25**, 85–90 (2017).
19. Han, X. Y., Gao, X., Zeng, D. L., Yan, J. & Li, J. M. Ratio of forbidden transition rates in the ground-state configuration of O II. *Phys. Rev. A* **85**, 062506 (2012).
20. Gao, X., Han, X. Y. & Li, J. M. Intimate relationship between spectroscopy and collisions: a scenario to calculate relevant atomic data for astrophysics. *J. Phys. B: At. Mol. Opt. Phys.* **49**, 214005 (2016).
21. Jönsson, P., He, X., Fischer, C. F. & Grant, I. P. The grasp2K relativistic atomic structure package. *Comput. Phys. Commun.* **177**, 597–622 (2007).
22. Jönsson, P., Gaigalas, G., Bieroń, J., Fischer, C. F. & Grant, I. P. New version: Grasp2K relativistic atomic structure package. *Comput. Phys. Commun.* **184**, 2197–2203 (2013).
23. Brown, G. V., Beiersdorfer, P., Chen, H., Chen, M. H. & Reed, K. J. Diagnostic Utility of the Relative Intensity of 3C to 3D in Fe XVII. *Astrophys. J.* **557**, L75–L77 (2001).
24. Graf, A., Beiersdorfer, P., Brown, G. V. & Gu, M. F. Measurement and Modeling of Na-Like Fe XVI Inner-Shell Satellites Between 14.5 Å and 18 Å. *Astrophys. J.* **695**, 818–824 (2009).
25. Breit, G. The effect of retardation on the interaction of two electrons. *Phys. Rev.* **34**, 553 (1929).
26. Grant, I. P. *Relativistic Quantum Theory of Atoms and Molecules*. (Springer-Verlag, New York, 2007).
27. Kramida, A., Ralchenko, Y. & Reader, J. NIST ASD Team, *NIST Atomic Spectra Database (version 5.6.1) [online]*. Available, <https://physics.nist.gov/asd> [Mon Feb 11 2019] National Institute of Standards and Technology (Gaithersburg, MD, 2019).
28. Gu, M. F. Indirect X-Ray Line-Formation Processes in Iron L-Shell Ions. *Astrophys. J.* **582**, 1241–1250 (2003).

29. Liu, Y., Yao, K., Hutton, R. & Zou, Y. Numerical simulations using an improved calculational scheme for ion charge state distribution and ion temperature evolution in an EBIT. *J. Phys. B: At. Mol. Opt. Phys.* **38**, 3207–3216 (2005).
30. Lu, X. J. & Currell, F. J. Numerical simulation of the charge balance and temperature evolution in an electron beam ion trap. *Phys. Rev. STAB* **12**, 014401 (2009).
31. Cagnac, B. & Pebay-Peyroula, J. C. *Modern Atomic Physics: Fundamental Principles*. (Macmillan Press, London, 1975).
32. Gao, X. & Li, J. M. Precision spectroscopy and electron-ion scattering. *Phys. Rev. A* **89**, 022710 (2014).
33. See the LCLS web page on SXR specifications, <https://lcls.slac.stanford.edu/instruments/sxr/specifications> (2019).
34. Schlotter, W. F. *et al.* The soft x-ray instrument for materials studies at the linac coherent light source x-ray free-electron laser. *Rev. Sci. Instrum.* **83**, 043107 (2012).
35. Inubushi, Y. *et al.* Determination of the Pulse Duration of an X-Ray Free Electron Laser Using Highly Resolved Single-Shot Spectra. *Phys. Rev. Lett.* **109**, 144801 (2012).
36. Behrens, C. *et al.* Few-femtosecond time-resolved measurements of X-ray free-electron lasers. *Nat. Commun.* **5**, 3762 (2014).
37. Hartmann, N. *et al.* Attosecond time-energy structure of X-ray free-electron laser pulses. *Nat. Photon.* **12**, 215–220 (2018).
38. Wu, C. & Gao, X. Resonance induced population transfer of Fe XVII ions in plasma environment. *J. Phys.: Conf. Ser.* **875**, 022011 (2017).
39. Wu, C., Chen, S., Chang, T. N. & Gao, X. Variation of the transition energies and oscillator strengths for the 3C and 3D lines of the Ne-like ions under plasma environment. Preprint at, <https://arxiv.org/abs/1904.08471> (2019).
40. Tiedtke, K. *et al.* Absolute pulse energy measurements of soft x-rays at the Linac Coherent Light Source. *Opt. Express* **22**, 21214–21226 (2014).
41. Chalupsky, J. *et al.* Comparing different approaches to characterization of focused X-ray laser beams. *Nucl. Instrum. Methods. A* **631**, 130–133 (2011).
42. Currell, F. (Eds) *Electron beam ion traps and their use in the study of highly charged ions, in The Physics of Multiply and Highly Charged Ions* (Vol. I) (Kluwer Academic, Dordrecht, 2003).

Acknowledgements

Parts of text in the introduction and conclusions were previously published in our conference proceeding paper. This work is supported by the National Natural Science Foundation of China (Grant Nos. 11774023 and U1530401), the National Key Research and Development Program of China (Grant No. 2016YFA0302104), the National High-Tech ICF Committee in China. We acknowledge the computational support provided by the Beijing Computational Science Research Center. We would like to acknowledge Prof. Tu-Nan Chang at University of Southern California for helpful discussions and comments of the manuscript.

Author Contributions

C.W. was responsible for most of the calculations and code development for the simulations. X.G. supervised the study. C.W. and X.G. drafted the manuscript.

Additional Information

Competing Interests: The authors declare no competing interests.

Publisher's note: Springer Nature remains neutral with regard to jurisdictional claims in published maps and institutional affiliations.



Open Access This article is licensed under a Creative Commons Attribution 4.0 International License, which permits use, sharing, adaptation, distribution and reproduction in any medium or format, as long as you give appropriate credit to the original author(s) and the source, provide a link to the Creative Commons license, and indicate if changes were made. The images or other third party material in this article are included in the article's Creative Commons license, unless indicated otherwise in a credit line to the material. If material is not included in the article's Creative Commons license and your intended use is not permitted by statutory regulation or exceeds the permitted use, you will need to obtain permission directly from the copyright holder. To view a copy of this license, visit <http://creativecommons.org/licenses/by/4.0/>.

© The Author(s) 2019